Bottom-up synthesis of 2D heterostructures enables effective polysulfides inhibition and conversion

Ge Zhang[1,§], Cheng Zhou[1,§], Juncai Long[1], Yan Li[1], Lei Lv[1], Kaijian Yan[1], Xinhui Chen[1], Chenxu Dong[2], Xu Xu[2] (✉), and Liqiang Mai[1] (✉)

[1] *State Key Laboratory of Advanced Technology for Materials Synthesis and Processing, Wuhan University of Technology, Wuhan 430070, China*
[2] *International School of Materials Science and Engineering, Wuhan University of Technology, Wuhan 430070, China*
[§] *Ge Zhang and Cheng Zhou contributed equally to this work.*

ABSTRACT

Due to the high theoretical capacity and energy density, lithium-sulfur (Li-S) batteries have good commercial prospects. However, shuttle effect of soluble lithium polysulfides (LiPSs) formed by sulfur reduction has severely limited the further development of Li-S batteries. In this work, the two-dimensional (2D) MXene-metal–organic framework (MOF) ($Ti_3C_2T_x$-CoBDC (BDC: 1,4-benzenedicarboxylate)) heterostructures were employed to modify the separator to inhibit the shuttle effect and facilitate the conversion of the soluble polysulfides. Firstly, a bottom-up synthesis strategy was adopted to synthesize the 2D MXene-MOF heterogeneous layered structure. With high specific surface area, in which the catalytic metal atoms not only restrain the shuttle effect of polysulfides but also exhibit excellent redox electrocatalytic performance. The cell with $Ti_3C_2T_x$-CoBDC@PP (PP: polypropylene) separator has a high initial capacity of 1255 mAh·g⁻¹ at 0.5 C. When the current density is 2 C, the battery has a capacity retention rate of 94.4% after 600 cycles, with the fading rate of only 0.01% per cycle. Besides, with a sulfur loading of 7.5 mg·cm⁻², the battery shows the discharge capacity of 1096 mAh·g⁻¹ at 0.2 C and exhibits excellent cycling stability. This work offers novel insights into the application of MOF and MXene heterostructures in Li-S batteries.

KEYWORDS

nanosheets, lithium-sulfur batteries, MXenes, modified separators, shuttle inhibition

1   Introduction

As global energy demand continues to increase, it has greatly contributed to the continuous innovation of advanced energy storage systems. However, the currently used lithium-ion battery has reached its theoretical energy density, which can not be able to meet the current needs. Lithium-sulfur (Li-S) batteries constructed from lithium metal anode and sulfur cathode exhibit an ultra-high theoretical energy density of 2600 Wh·kg⁻¹ [1–5]. In addition, Li-S batteries benefit from abundant sulfur content resources, environmental friendliness, low price, and non-toxicity [6, 7]. Nevertheless, the widespread use of Li-S batteries has some urgent problems to be solved, such as sulfur inferior conductivity as well as its final discharge products, large volume expansion during cycling, and the shuttle effect of soluble lithium polysulfides (LiPSs). The shuttle effect not only induces the loss of active sulfur cathode and the corrosion of lithium metal anode, but also the low Coulombic efficiency (CE) and poor cycling stability [8–12].

Separator, as an indispensable part of the battery system, separates the cathode and anode to prevent short-circuiting of the battery, while providing a channel for ion transport. Polyolefin separators are widely used due to their superior mechanical properties, outstanding chemical stability and high porosity. The microscopic size of long-chain LiPSs is much narrower than the pore size of conventional separator, which can not physically resist the shuttle of the LiPSs, resulting in the destruction of cathode active material and severe side reactions on the anode [13–15]. Therefore, separator modification is one of the simplest and most effective ways to retard the shuttle effect of LiPSs. Exploring materials that can simultaneously adsorb and catalyze LiPSs can be great help for separator modification.

Metal–organic frameworks (MOFs) contain metal ions and organic ligands, which have been widely investigated for their ample metal active centers, large specific surface area, highly ordered pores, and adjustable pore size. The presence of Lewis acidic metal sites in MOFs can strongly interact with polysulfide anions, so alleviating the shuttle effect of LiPSs [16–20]. Yang and co-workers synthesized π–d conjugated Ni-MOF-1D (1D: one-dimensional), which has a strong ability to trap the soluble LiPSs. Meanwhile, the π–d structure exhibits excellent electrical conductivity [21]. Wu et al. coated CNT@ZIF (CNT: carbon nanotube, ZIF: zeolitic imidazolate framework) on the polypropylene (PP) separator and successfully confined the LiPSs to the cathode side by using Lewis acid-base interaction of ZIF-8 with LiPSs [22]. However, MOFs have poor electrical conductivity, and tend to aggregate and collapse structurally during the charging and discharging process, resulting in a rapid decline of specific surface area. Assembling MOF on a conductive two-dimensional material is a favorable solution [23–25].

MXene refers to a class of transition metal carbide/nitride

materials featuring a two-dimensional structure, excellent electrical conductivity, large active surface, and Lewis acidic surface, which makes it promising for catalytic and energy storage applications [26–31]. The terminals on the surface of MXene exhibit strong adsorption to LiPS and form strong metal–S bonds to inhibit shuttle effects. In addition, MXene with abundant terminals exhibits an effective catalytic effect on the conversion between LiPS and Li_2S, thus promoting the redox kinetics during cycling [32–36]. For example, Jiao and co-workers have successfully fabricated TiO_2-MXene ($Ti_3C_2T_x$) heterostructures, which promoted the catalytic conversion of polysulfides and effectively enhanced the cycling life of Li-S batteries [37]. Then, Zhang and co-workers used MXene and Ktejen black to form interwoven KB@$Ti_3C_2T_x$ composites to modify the separators, which greatly enhanced the practicality of Li-S batteries [38]. Besides, the van der Waals forces and hydrogen bonding caused the stacking of MXene sheets, which resulted in a significant loss of active surface area [39–41]. Therefore, it is necessary to solve the stacking of MXene sheets to maximize the use of their active surfaces.

Herein, the two-dimensional (2D) MXene-MOF ($Ti_3C_2T_x$-CoBDC) (BDC: 1,4-benzenedicarboxylate) composites were designed and synthesized for separator modification. The Co-MOF was *in situ* grown on the MXene nanosheets via the bottom-up synthesis strategy. In this dual function composite structure, the MXene nanosheets enabled improved the electrical conductivity and accelerated the conversion of LiPSs. At the same time, the existence of Co-MOF improves the capture of polysulfide and effectively prevents the large surface area loss caused by stacking of MXene nanosheets. As a result, the $Ti_3C_2T_x$-CoBDC multifunctional layer demonstrated strong adsorption and catalysis ability towards LiPSs, which efficiently inhibits the shuttle effect and enhances the sulfur utilization. Due to the synergic effect, the batteries with the functional separators not only exhibit the discharge capacity of 1255 mAh·g^{-1} at 0.5 C, but also feature extremely long cycle stability (600 cycles at 2 C with capacity retention of 94.4%). Moreover, at a sulfur loading of 7.5 mg·cm^{-2}, the battery shows the discharge capacity of 1096 mAh·g^{-1} at 0.2 C and exhibits excellent cycling stability.

2 Experimental section

2.1 Synthesis of MXene ($Ti_3C_2T_x$)

MXene nanosheets were prepared by etching the Ti_3AlC_2. Specifically, 2 g Ti_3AlC_2 was slowly added to 20 mL hydrofluoric acid (HF) solution and stirred slowly for 24 h. The obtained solution was centrifuged at 10,000 rpm for 3 min and washed several times with deionized water until the pH reached 6. The precipitate obtained by centrifugation was transferred to a glass bottle with tetramethylammonium hydroxide and stirred for 10 days. The solution after 10 days of reaction was centrifuged and washed with deionized water, and the precipitate was transferred to a four-mouth flask and sonicated with a cell grinder. Take suspension and freeze-dry it for 48 h to obtain a few-layer of MXene nanosheets.

2.2 Synthesis of CoBDC

$Co(CH_3COO)_2 \cdot 4H_2O$ and 1,4-BDC were used as precursors. Specifically, 50 mg of 1,4-BDC was added to a mixture of 2 mL N,N-dimethylformamide (DMF) and 1 mL CH_3CN, stirred for 5 min to dissolve completely, and then poured to the bottom of the test tube. Then 1 mL of DMF and 1 mL of CH_3CN were added to the test tube as the intermediate layer of the reaction. Finally, 50 mg of $Co(CH_3COO)_2 \cdot 4H_2O$ was added to 1 mL of DMF and 2 mL of CH_3CN, stirred until completely dissolved, and

then the solution was added to the top of the test tube. At this time, the solution was stratified and left to react for 24 h. The precipitate at the bottom of the test tube was centrifuged at 10,000 rpm for 3 min and washed with DMF and CH_2Cl_2, respectively. The precipitate obtained after centrifugation was placed in a vacuum drying oven at 60 °C for 24 h to obtain CoBDC.

2.3 Synthesis of $Ti_3C_2T_x$-CoBDC

The synthesis of $Ti_3C_2T_x$-CoBDC was similar to that of CoBDC, except that MXene nanosheets and $Co(CH_3COO)_2 \cdot 4H_2O$ were dissolved together in a mixture of 1 mL of DMF and 2 mL of CH_3CN, and the mixed solution was placed on the top of the test tube.

2.4 Preparation of $Ti_3C_2T_x$-CoBDC@PP separator

Approximately 2 mg of $Ti_3C_2T_x$-CoBDC was dissolved in 60 mL of ethanol and sonicated, and the prepared dispersion was vacuum filtered on a PP separator. The loading of $Ti_3C_2T_x$-CoBDC was 0.1 mg·cm^{-2}. The filtered separator was dried in a vacuum drying oven at 60 °C for one day. $Ti_3C_2T_x$@PP and CoBDC@PP were obtained using the same method.

2.5 Preparation of S/reduced graphene oxide (rGO) cathode

1.5 mg of graphene oxide, 0.069 mL sodium thiosulfate (1 mol·L^{-1}), and 0.069 mL hydrochloric acid (2 mol·L^{-1}) were mixed in deionized water to obtain 1.4 mL solution in a vial. After reacted at 95 °C for 2 h, the obtained hydrogel was washed for three times by deionized water and then freeze-dried to get the freestanding S/rGO composite. The areal loading of S/rGO depended on the molar mass of sodium thiosulfate and hydrochloric acid. The sulfur loading was 2.5 mg·cm^{-2} for the routine electrochemical performance test. The preparation of high sulfur loading cathodes with 7.5 mg·cm^{-2} required increasing the amount of sodium thiosulfate to 0.19 mL and increasing hydrochloric acid in corresponding proportion. We conducted thermogravimetric (TG) test on sulfur cathode, and the sulfur loading of normal sulfur cathode was 60% (Fig. S1 in the Electronic Supplementary Material (ESM)).

2.6 Materials characterization

Scanning electron microscopy (SEM, JEOL JSM-7100F), transmission electron microscopy (TEM), and high-resolution TEM (HRTEM, Titan G2 60-300) were used for structural, morphological, and elemental characterization of the samples. X-ray diffraction (XRD) patterns of samples were performed on D8 Advance X-ray diffractometer with a non-monochromated Cu Kα X-ray source (λ = 1.054056 Å). X-ray photoelectron spectroscopy (XPS) was carried out using an ESCALAB 250Xi instrument. The atomic force microscopy (AFM) was performed into this sample using a Nanoscope VMultimode 8 scanning probe microscope from Bruker Corporation. *In/ex situ* Raman spectra were recorded using a HORIBA HR EVO Raman system with an excitation wavelength of 532 nm.

2.7 Separator characterization

The dynamic contact angle measurements were conducted using an optical contact angle measuring and contour analysis system (Dataphysics DCA 35). The heat resistance was tested by using an infrared thermal imager (FLIR T429) with a temperature range from 30 to 120 °C.

2.8 Shuttle test

Li_2S_6 was configured by adding a mixture of 1,2-dimethoxyethane (DME) and 1,3-dioxane (DOL) (1:1 by volume) of sulfur and Li_2S

in a molar ratio of 5:1, and stirred vigorously at 70 °C for 48 h to homogenize it. Then the same volume of Li_2S_6 solution and blank solution was added on each side of the proton exchanger vessel and tested.

2.9 Measurement for the nucleation of lithium sulfide

Li_2S_8 electrolyte was prepared using the same method as Li_2S_6. $Ti_3C_2T_x$-CoBDC, $Ti_3C_2T_x$ and CoBDC were coated on aluminum foil as cathode. Celgard 2500 as separator, Li metal as anode, and coated material as cathode were used to assemble CR2025 coin cell. Specifically, during the battery assembly, Li_2S_8 was dripped onto the cathode, and then the electrolyte without Li_2S_8 was dripped onto the lithium anode side. The lithium-catalyst batteries were galvanostatically discharged at 0.112 mA to 2.06 V, and then the potential was held at 2.05 V until the current dropped below 10^{-5} A. When the overpotential was 0.01 V, Li_2S was deposited and grown on the surface of the cathode material. The nucleation rate of Li_2S can be calculated by Faraday's law.

2.10 Electrochemical measurement

The 2025-type coin cells were assembled in a glovebox filled with pure argon gas (H_2O < 0.1 ppm and O_2 < 0.1 ppm). A Celgard 2500 PP was used as the normal separator, the $Ti_3C_2T_x$-CoBDC@PP and $Ti_3C_2T_x$@PP as functional separators. The electrolyte was a solution of 1 M lithium bis(trifluoromethanesulfonyl)-imide (LiTFSI) in (1:1) DME and DOL, and $LiNO_3$ (1 wt.%) was severed as an additive. The amount of electrolyte was related to the active sulfur, and the ratio of electrolyte to S was 20 (μL):1 (mg). The galvanostatic charge–discharge test was carried on a NEWARE battery tester in voltage range between 1.7 and 2.8 V. The cycle cyclic voltammetry (CV) curves and electrochemical impedance spectroscopy tests (0.1 Hz–100 kHz, 5 mV) were conducted on an electrochemical workstation (Autolab PGSTAT302N).

2.11 *In situ* Raman spectroscopy measurements

In situ Raman spectroscopy was performed using a Li-S coin cell with a negative shell with a quartz window. A hole (5 mm) was punched on Li-metal anode to allow the laser to shine on the separator directly. The Raman signal was recorded using a HORIBA HR EVO Raman system (532 nm laser).

3 Results and discussion

Figure 1 illustrates the synthetic route to the $Ti_3C_2T_x$-CoBDC. The accordion shaped $Ti_3C_2T_x$ MXene is acquired through HF etching the metallic Al layer in Ti_3AlC_2. The few-layer layers of $Ti_3C_2T_x$ nanosheets can be obtained after tetramethylammonium hydroxide intercalation treatment and then delamination using

ultrasound [42]. The obtained $Ti_3C_2T_x$ nanosheets are then used as the synthetic template for the *in situ* deposition of CoBDC, and a bottom-up synthesis strategy is employed to prepare $Ti_3C_2T_x$-CoBDC nanosheets [43]. The DMF and CH_3CN are used as the reaction solvents to form three liquid phase layers in appropriate proportions, which are arranged vertically at different densities. The top solution contains Co^{2+} and $Ti_3C_2T_x$ nanosheets, and the bottom solution contains 1,4-BDC, separated by an intermediate solvent layer. The presence of negatively charged groups (like –O, –OH, and –F) in MXene allows it to combine with positively charged cobalt ions through electrostatic interaction. Under static conditions, the Co^{2+} cations in the top layer, $Ti_3C_2T_x$ nanosheets, and the 1,4-BDC linkers in the bottom all diffuse to the middle region and form CoBDC by *in situ* growth on MXene nanosheets.

SEM and TEM technologies were used to investigate the morphology and structure of $Ti_3C_2T_x$-CoBDC (Figs. 2(a) and 2(b)). $Ti_3C_2T_x$-CoBDC displays a sheet-like morphology but a rough surface due to the formation of CoBDC on the surface of $Ti_3C_2T_x$. The HRTEM picture of the hybridized nanosheets reveals that CoBDC homogeneously distributed on $Ti_3C_2T_x$ (Fig. 2(c)). High-angle annular dark-field scanning transmission electron microscopy (HAADF-STEM) elemental mapping analysis shows that elements Ti, Co, C, and N are uniformly distributed throughout the nanosheets (Fig. 2(d)), which further confirms the uniform growth of CoBDC on $Ti_3C_2T_x$ nanosheet.

XRD pattern shows that the (002) peak of Ti_3AlC_2 MAX phase shifts from 9.7° to the diffraction peak of $Ti_3C_2T_x$ at (002) at 6.2° after HF etching, while the (104) diffraction peak disappears (Fig. S2 in the ESM), indicating that the metallic Al layer is removed [44]. The Al 2p XPS spectra before and after Ti_3AlC_2 etching show that the Al layer is completely removed after etching, which is consistent with the XRD results (Fig. S3 in the ESM). The diffraction peaks of CoBDC are at 8.8°, 15.7°, and 17.8°, which are consistent with previous reports. Four distinct diffraction peaks of $Ti_3C_2T_x$-CoBDC correspond to the (002) crystal plane of $Ti_3C_2T_x$, (200), (20$\bar{1}$), and (400) planes of CoBDC (Figs. 2(e) and 2(f)) [45]. The Fourier transform infrared spectroscopy (FT-IR) spectrum of the $Ti_3C_2T_x$-CoBDC is shown in Fig. 2(g). The appearance of the peaks at 810 and 1425 cm^{-1} is attributed to the vibration of the benzene ring. The two characteristic peaks at 1270 (C–O) and 1575 cm^{-1} (O–C=O) are attributed to the vibration of the benzodicarboxylic acid anion respectively, indicating the successful synthesis of CoBDC on the surface of $Ti_3C_2T_x$. The structures of $Ti_3C_2T_x$, CoBDC, and $Ti_3C_2T_x$-CoBDC were further characterized by Raman spectroscopy (Fig. S4 in the ESM). Specifically, the spectrum of $Ti_3C_2T_x$ shows a peak at about 155 cm^{-1} and CoBDC shows a peak at 673 cm^{-1}, both of which are detected in the Raman spectrum of $Ti_3C_2T_x$-CoBDC. The successful complexation of CoBDC with $Ti_3C_2T_x$ was further
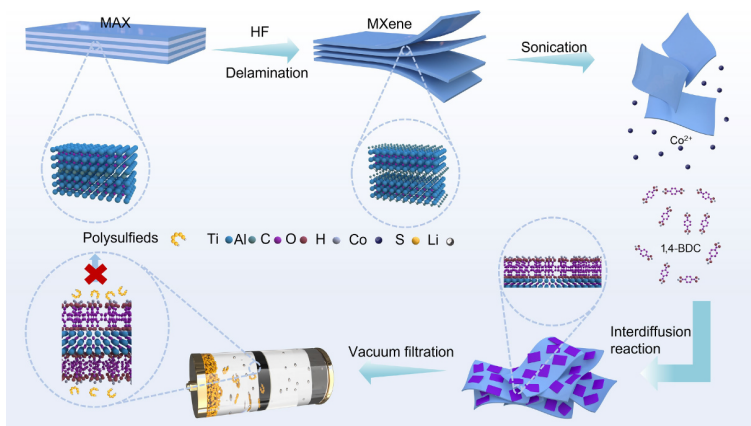

Figure 1 Synthesis process illustration of $Ti_3C_2T_x$-CoBDC, and its working mechanism in lithium-sulfur battery.
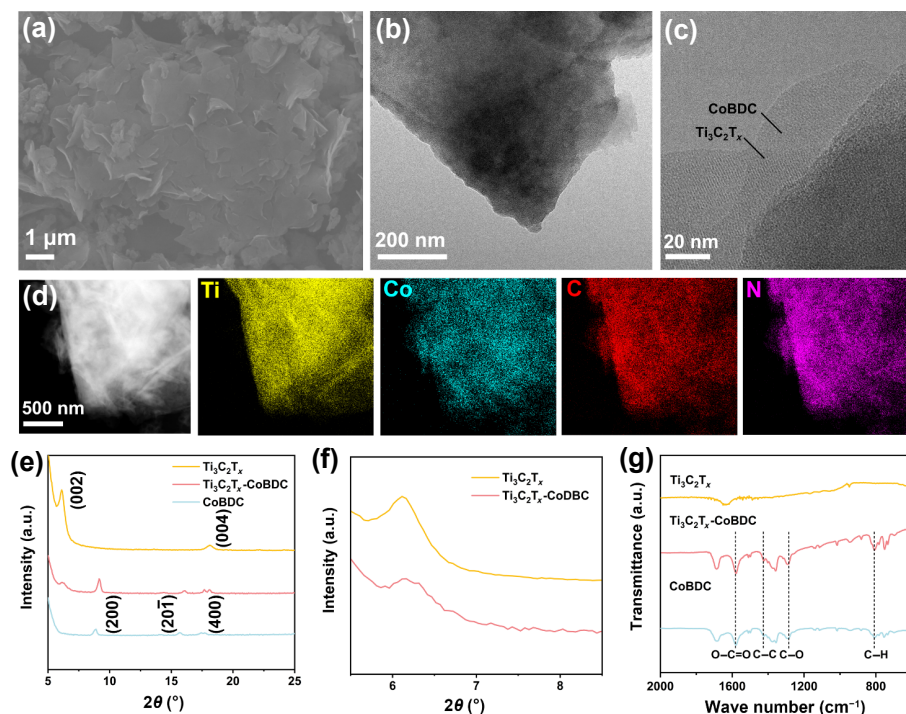
Figure 2 (a) SEM image, (b) TEM image, (c) HRTEM image, (d) HAADF-STEM image and the corresponding energy dispersive spectroscopy (EDS) elemental mappings of $Ti_3C_2T_x$-CoBDC. (e) XRD patterns of the $Ti_3C_2T_x$, $Ti_3C_2T_x$-CoBDC, and CoBDC, and (f) magnified XRD patterns showing the 2θ region from 5° to 8°. (g) FT-IR spectra of the $Ti_3C_2T_x$, $Ti_3C_2T_x$-CoBDC, and CoBDC.

demonstrated, which matches well with the previous XRD analysis results. In order to accurately characterize the morphological features of the $Ti_3C_2T_x$-CoBDC, the thickness of the $Ti_3C_2T_x$-CoBDC was characterized using AFM. The experimental results show that the thickness of the $Ti_3C_2T_x$-CoBDC is about 4.8 nm (Fig. S5 in the ESM).

The $Ti_3C_2T_x$-CoBDC@PP separator was prepared by filtration, and the surface SEM image shows that $Ti_3C_2T_x$-CoBDC was uniformly dispersed on the PP separator (Fig. S6 in the ESM). The thickness of $Ti_3C_2T_x$-CoBDC layer on the PP separator is 5 μm as shown in the cross-sectional SEM image (Fig. 3(a)). After bending

the $Ti_3C_2T_x$-CoBDC@PP under different stresses, $Ti_3C_2T_x$-CoBDC adhered well to the PP separator after bending without obvious signs of shedding, indicating that $Ti_3C_2T_x$-CoBDC@PP has good mechanical properties (Fig. 3(b)). The wettability of the electrolyte on the separator is also critical. As illustrated in Fig. 3(c), the contact angle of electrolyte on the surface of $Ti_3C_2T_x$-CoBDC@PP separator is about 0°, which is smaller than $Ti_3C_2T_x$@PP (contact angle is 26.6°) and PP (contact angle is 46.3°) separators, indicating that the $Ti_3C_2T_x$-CoBDC@PP separator has better electrolyte wettability, facilitating the ionic transport. To examine the thermal stability of the separator, Fig. S7 in the ESM shows the
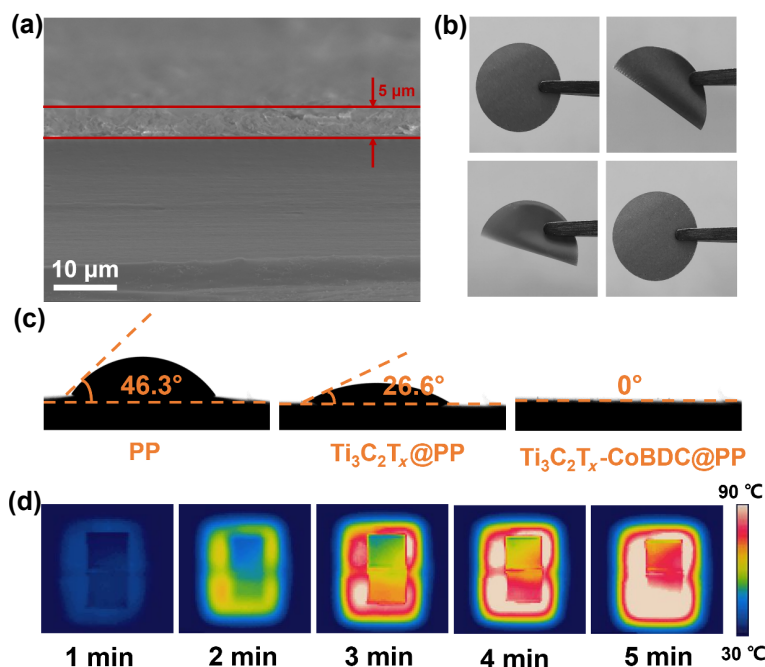

Figure 3 (a) The cross-sectional SEM image of $Ti_3C_2T_x$-CoBDC@PP separator. (b) Digital photos of $Ti_3C_2T_x$-CoBDC@PP separator under various stresses. (c) Contact angle measurements with electrolyte of PP, $Ti_3C_2T_x$@PP, and $Ti_3C_2T_x$-CoBDC@PP, respectively. (d) The heat resistance of $Ti_3C_2T_x$-CoBDC@PP (up) and PP (down) separators at 120 ℃.

optical photographs of the three separators, $Ti_3C_2T_x$-CoBDC@PP, $Ti_3C_2T_x$@PP, and PP before and after heat treatment at 120 °C for 2 h. PP separator underwent significant deformation after heat treatment, and the surface of $Ti_3C_2T_x$@PP peeled off severely, while the $Ti_3C_2T_x$-CoBDC@PP showed no significant difference after heat treatment. Moreover, the temperature difference of the separator surface when the heater was heated to 120 °C was recorded with an infrared thermographic camera. As shown in Fig. 3(d), during the heating process, $Ti_3C_2T_x$-CoBDC@PP exhibits a slower heat transfer compared to PP separator, indicating its good thermal resistance. As a result, the safety is also better during the battery cycling process.

Adsorption ability towards LiPSs is important because it can effectively suppress the shuttle effect. To verify the trapping ability of $Ti_3C_2T_x$-CoBDC, visual adsorption experiments were employed to investigate the trapping ability of $Ti_3C_2T_x$-CoBDC and control samples in Li_2S_6 solution. The different adsorption abilities between $Ti_3C_2T_x$-CoBDC and $Ti_3C_2T_x$ are shown in Fig. 4(a). In the ultraviolet/visible (UV–vis) spectra, it can be seen that the Li_2S_6 peaks of $Ti_3C_2T_x$ and $Ti_3C_2T_x$-CoBDC weaken sequentially, indicating that their adsorption capacities of Li_2S_6 are higher [46, 47], which is responsible for the dual effect of the large specific surface area of $Ti_3C_2T_x$ and the abundant unsaturated sites of CoBDC. Meanwhile, the separators should have high ion selectivity to inhibit the crossover of soluble polysulfides, thus eliminating a series of side effects on the lithium anode. To investigate the shielding effect of $Ti_3C_2T_x$-CoBDC on polysulfide, visualization experiments of polysulfide shielding using a proton exchanger vessel were performed. As for the PP separator, the polysulfide crossover became more and more obvious, indicating poor polysulfide blocking ability. In comparison, $Ti_3C_2T_x$@PP solution did not change color as dark as PP. In contrast, $Ti_3C_2T_x$-CoBDC@PP still did not show significant shuttle after 24 h, demonstrating the superior polysulfide inhibition ability (Fig. S8 in the ESM). The results verify the high ion selectivity of $Ti_3C_2T_x$-CoBDC for soluble polysulfides.

The surface chemical interactions of $Ti_3C_2T_x$-CoBDC after the interactions of Li_2S_6 were further investigated by XPS. As shown in Fig. 4(b), the Co 2p spectrum contains Co 2p3/2 and Co 2p1/2 components, each of which can decompose to Co^{3+}, Co^{2+}, and satellite peaks. The Co 2p and Ti 2p (Fig. S9 in the ESM) clearly move toward a lower binding energy after interaction with Li_2S_6. Figure 4(c) shows the high-resolution S 2p spectrum, where the terminal sulfur (S_T–S_T) and bridging sulfur (S_B–S_B) peaks can be seen. Furthermore, the peaks at 169.2 and 167.9 eV are polysulfide ion complexes. The XPS spectrum shows the electron transfer of $Ti_3C_2T_x$-CoBDC, demonstrating its interaction with Li_2S_6 [48]. Figure 4(d) reveals the CV of Li-S cells with different separators at 0.1 mV·s⁻¹. The two cathodic peaks around 2.3 and 2.0 V correspond to the reduction of S_8 to long-chain LiPSs (Li_2S_x ($4 \leq x \leq 6$)) and then the final formation of Li_2S_2/Li_2S, respectively, while the anodic peak around 2.4 V represents the opposite
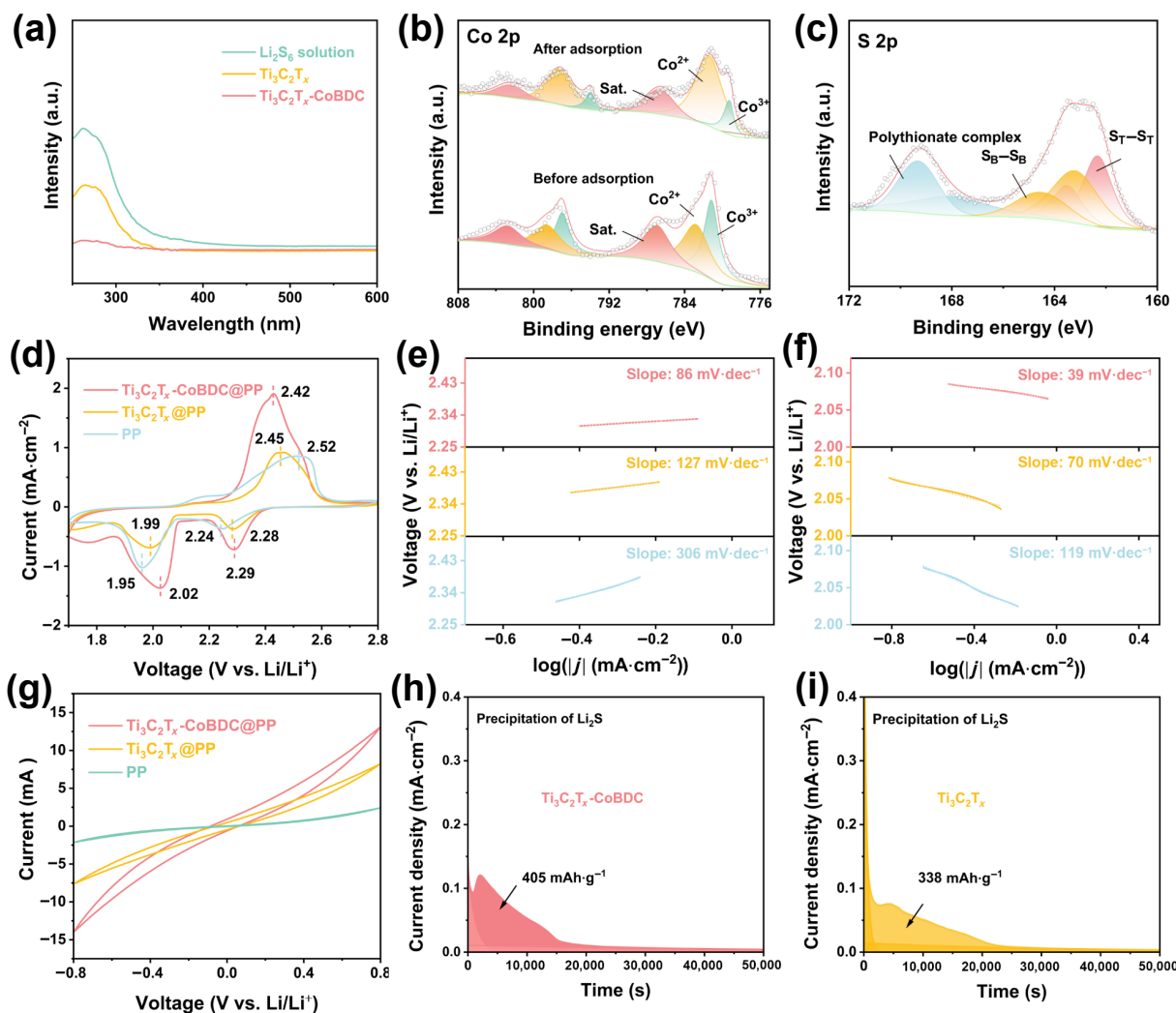

Figure 4 (a) UV–vis absorption spectra of Li_2S_6 solution after the addition of $Ti_3C_2T_x$, CoBDC, and $Ti_3C_2T_x$-CoBDC, respectively. (b) Co 2p XPS spectra, and (c) S 2p XPS spectrum of $Ti_3C_2T_x$-CoBDC before and after Li_2S_6 adsorption. (d) CV curves, ((e) and (f)) Tafel slopes from the cathodic peaks of the CV curves. (g) CV curves of symmetric cells at 30 mV·s⁻¹. Precipitation profiles of Li_2S with (h) $Ti_3C_2T_x$-CoBDC and (i) $Ti_3C_2T_x$, respectively.

process. The cell with Ti$_3$C$_2$T$_x$-CoBDC@PP separator has a maximum peak current at 2.42 V and also has the smallest polarization curve, which confirms its accelerated redox kinetics and favors the conversion of LiPSs. The Tafel slopes corresponding to the CV results are shown in Figs. 4(e) and 4(f). The cell with Ti$_3$C$_2$T$_x$-CoBDC@PP separator shows smaller Tafel slopes for both the reduction of S$_8$ to long-chain LiPSs (Li$_2$S$_x$ ($4 \leq x \leq 6$)) and the formation of Li$_2$S$_x$/Li$_2$S. The apparent difference in Tafel slopes demonstrates the rapid oxidation of Ti$_3$C$_2$T$_x$-CoBDC modified separator after the assembly of the cell reduction reaction kinetics. For the further understanding of the catalytic activity toward LiPSs in several modified separators, symmetric cells with Li$_2$S$_6$ were assembled and tested. As shown in Fig. 4(g), the current response of the symmetric cells assembled with three separators, Ti$_3$C$_2$T$_x$-CoBDC@PP, Ti$_3$C$_2$T$_x$@PP, and PP, decreases in order, verifying that Ti$_3$C$_2$T$_x$-CoBDC@PP has good catalytic activity and accelerates the kinetics of the redox reaction during the reaction. To further verify that Ti$_3$C$_2$T$_x$-CoBDC can enhance the kinetics of redox reactions, nucleation experiments were performed. As shown in Figs. 4(h) and 4(i), the nucleation experiment exhibit that the capacity of Li$_2$S precipitated on Ti$_3$C$_2$T$_x$-CoBDC is 405 mAh·g^{-1}, exceeding Ti$_3$C$_2$T$_x$ (338 mAh·g^{-1}). Ti$_3$C$_2$T$_x$-CoBDC also shows the highest peak current, indicating that Ti$_3$C$_2$T$_x$-CoBDC effectively promotes Li$_2$S nucleation on the electrode surface.

Electrochemical performance test results of cells with three separators were obtained. The results of three separators at 0.5 C are shown in Fig. 5(a). Attributed to the catalytic effect of MXene,

the cells with Ti$_3$C$_2$T$_x$-CoBDC@PP and Ti$_3$C$_2$T$_x$-@PP separators exhibit faster chemical reaction kinetics. Therefore, they exhibit higher capacity in the initial stage. After 3 cycles of activation at 0.2 C, the cell with Ti$_3$C$_2$T$_x$-CoBDC@PP separator shows stable cycling performance attributed to better adsorption of polysulfides by the Co metal center. The cell with Ti$_3$C$_2$T$_x$-CoBDC@PP separator also delivers the highest discharge specific capacity of 1255 mAh·g^{-1} at 0.5 C and 82% capacity retention after 100 cycles. Instead, the cells with Ti$_3$C$_2$T$_x$@PP and PP separators exhibit lower capacities of 1076 and 997 mAh·g^{-1}, respectively. And the cells also show faster capacity decay during cycling. Figure 5(b) displays the rate performance of the cell at different current densities. It can be seen that the battery with Ti$_3$C$_2$T$_x$-CoBDC@PP separator performs outstandingly. The reversible discharge capacities of the cells using Ti$_3$C$_2$T$_x$-CoBDC@PP separator are 1333, 1070, 803, and 654 mAh·g^{-1} at current densities of 0.5, 1, 2, and 3 C, respectively. Fast charging and discharging processes at high current densities require fast catalytic conversion activity. Due to Ti$_3$C$_2$T$_x$ having high catalytic activity for polysulfides, the cell with Ti$_3$C$_2$T$_x$-CoBDC@PP separator demonstrates high reversible capacity at high rates. In comparison, the cells with Ti$_3$C$_2$T$_x$@PP and PP separators exhibit poor rate performance and low discharge capacity. Figure 5(c) and Fig. S10 in the ESM show the galvanostatic charge/discharge profiles of the cells at different current densities from 0.5 to 3 C. The two discharge plateaus of the cell with Ti$_3$C$_2$T$_x$-CoBDC@PP separator at a current density of 3 C are still maintained, suggesting the fast catalytic conversion reaction of LiPSs. The cells with Ti$_3$C$_2$T$_x$@PP and PP separators
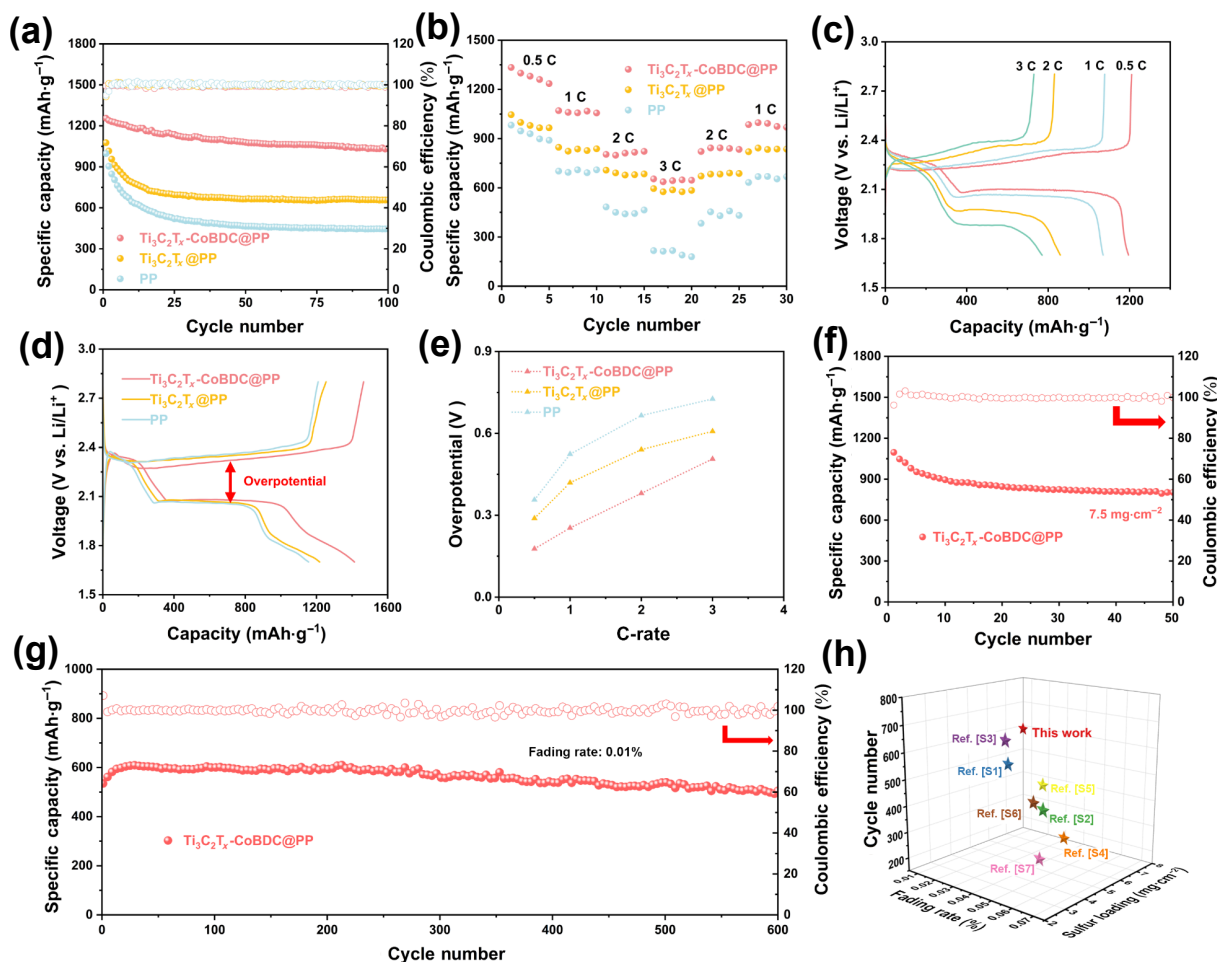

Figure 5 Electrochemical performances of the Li-S cells with different separators. (a) Cycling test at 0.5 C. (b) Rate performance. (c) Galvanostatic charge–discharge profiles of the Li-S cell with Ti$_3$C$_2$T$_x$-CoBDC@PP separator at different rates. (d) Galvanostatic charge–discharge profiles at 0.2 C in potential window from 1.7 to 2.8 V. (e) The over potential at different rates. (f) Cycling stability under high sulfur loading. (g) Long-term performance of Ti$_3$C$_2$T$_x$-CoBDC@PP separator at a current density of 2 C. (h) A comparison with other works about separators modified by MXene-based materials.

have less pronounced voltage plateaus and lower capacity at higher current densities. As shown in Fig. 5(e), the polarization voltages of the cell with $Ti_3C_2T_x$-CoBDC@PP (0.61 V) and PP (0.73 V) separators are higher than that of the cell with $Ti_3C_2T_x$-CoBDC@PP separator (0.51 V) at a high rate of 3 C. Besides, the cell with $Ti_3C_2T_x$-CoBDC@PP separator also exhibits the lowest polarization potential at 0.2 C, demonstrating the excellent catalytic effect of $Ti_3C_2T_x$-CoBDC on the redox of LiPSs (Fig. 5(d)).

The batteries with $Ti_3C_2T_x$-CoBDC@PP separators were assembled to specifically evaluate the long-cycle performance of the batteries. The initial discharge capacity of the battery is 534 mAh·g^{-1} when the current density is 2 C, and the capacity of the battery remains around 504 mAh·g^{-1} after 600 cycles, with a corresponding capacity retention rate of 94.4% and the fading rate was only 0.01% per cycle (Fig. 5(g)). For further development of Li-S batteries, their cycling performance under high sulfur loading is important. Therefore, the performance of cells with $Ti_3C_2T_x$-CoBDC@PP separator at a sulfur loading of 7.5 mg·cm^{-2} was tested. The initial discharge capacity of the cell is up to 1096 mAh·g^{-1} at 0.2 C, and the cell maintained good cycling stability (Fig. 5(f)). Moreover, the CE of $Ti_3C_2T_x$-CoBDC@PP is basically stable at 99.8%, showing the excellent cycling stability under the high sulfur loading condition. Figure 5(h) and Table S1 in the ESM show the comparison of this work with previously reported MXene based materials, in which the separator in this work shows clear advantages in terms of high sulfur loading and cycling stability. These results further indicate that $Ti_3C_2T_x$-CoBDC has a strong catalytic conversion capacity, high sulfur utilization, and excellent cycle stability during the cycling process.

In situ Raman spectroscopy was further used to explore the conversion process of various LiPSs during charging/discharging. It is also applied to verify the advantages of $Ti_3C_2T_x$-CoBDC heterogeneous layered structure as a multifunctional coating in the battery cycling process. The signals of long-chain and medium-chain LiPSs are clearly visible for the cell with PP separator. The signals of long-chain LiPSs start to appear at the beginning of discharge, with peaks at 148, 218, and 470 cm^{-1} are seen as the characteristic Raman peaks of Li_2S_8. The Raman peaks at 399 and 452 cm^{-1} are the long-chain LiPSs Li_2S_5, Li_2S_4, and Li_2S_6, respectively. These two characteristic peaks appear at the second plateau (2.1 V) during the discharge and persist until the end [49–51]. It is thus clear that a severe shuttle effect occurs in LiPSs as shown in Figs. 6(a) and 6(b). In sharp contrast, Figs. 6(c) and 6(d) show that the cell with $Ti_3C_2T_x$-CoBDC@PP separator exhibits almost no characteristic peaks during the whole discharge process. This implies that the dissolved LiPSs can be effectively captured by $Ti_3C_2T_x$-CoBDC@PP during the discharge process, which greatly alleviates the shuttle of lithium polysulfide. Similarly, the variation of peak intensity of different LiPSs during the charging process can be observed for different separators (Fig. S11 in the ESM).

4   Conclusions

In summary, the bottom-up approach enabled the $Ti_3C_2T_x$-CoBDC heterogeneous layered structure to be successfully prepared and its use in separator modification. Compared with $Ti_3C_2T_x$ and CoBDC alone, the $Ti_3C_2T_x$-CoBDC heterogeneous layered structure enhances the adsorption and catalytic ability of polysulfides. Combined with various experiments, it is verified that CoBDC has a strong adsorption ability for polysulfides, and $Ti_3C_2T_x$ has a better catalytic ability on polysulfides as well as excellent electrical conductivity, accelerating the conversion of intercepted polysulfides. These synergistic advantages allow cells assembled with $Ti_3C_2T_x$-CoBDC@PP separators to perform well in rate capacity and long-term cycling. The battery assembled with $Ti_3C_2T_x$-CoBDC@PP separator has an impressive initial capacity of up to 1255 mAh·g^{-1} at 0.5 C. When the current density is 2 C, the battery has a capacity retention rate of 94.4% after 600 cycles, with the fading rate was only 0.01% per cycle. Besides, at a sulfur loading of 7.5 mg·cm^{-2}, the battery shows the discharge capacity of 1096 mAh·g^{-1} at 0.2 C with excellent cycling stability. This work
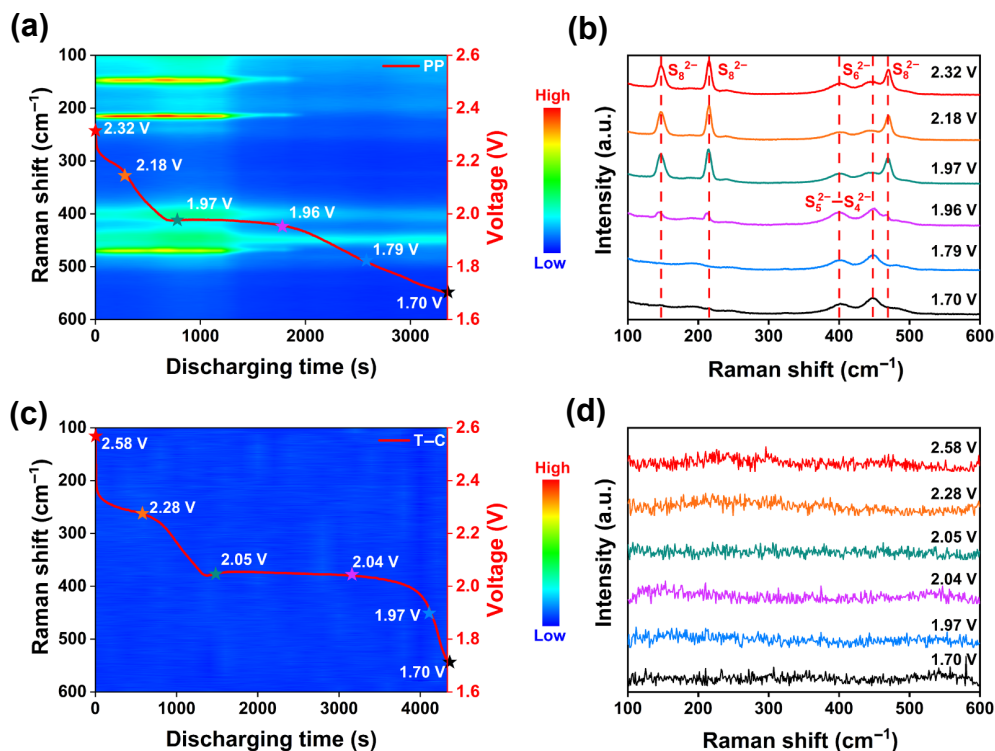

Figure 6 *In situ* Raman spectra and *in situ* time-resolved Raman spectra tested during the discharging processes of the cells with ((a) and (b)) PP and ((c) and (d)) $Ti_3C_2T_x$-CoBDC@PP separator.

may provide new development opportunities for MOF and MXene heterostructures in separator modification and inspire the exploration of high-performance Li-S batteries.

Acknowledgements

Electronic Supplementary Material: Supplementary material (further details of SEM imaging, Raman spectroscopy measurements, and XPS spectra) is available in the online version of this article at https://doi.org/10.1007/s12274-023-5535-z.

References

[1] Bruce, P. G.; Freunberger, S. A.; Hardwick, L. J.; Tarascon, J. M. Li-O_2 and Li-S batteries with high energy storage. *Nat. Mater.* **2012**, *11*, 19–29.

[2] Lei, T. Y.; Chen, W.; Lv, W. Q.; Huang, J. W.; Zhu, J.; Chu, J. W.; Yan, C. Y.; Wu, C. Y.; Yan, Y. C.; He, W. D. et al. Inhibiting polysulfide shuttling with a graphene composite separator for highly robust lithium-sulfur batteries. *Joule* **2018**, *2*, 2091–2104.

[3] Pang, Q.; Liang, X.; Kwok, C. Y.; Nazar, L. F. Advances in lithium-sulfur batteries based on multifunctional cathodes and electrolytes. *Nat. Energy* **2016**, *1*, 16132.

[4] Xu, J.; An, S. H.; Song, X. Y.; Cao, Y. J.; Wang, N.; Qiu, X.; Zhang, Y.; Chen, J. W.; Duan, X. L.; Huang, J. H. et al. Towards high performance Li-S batteries via sulfonate-rich COF-modified separator. *Adv. Mater.* **2021**, *33*, 2105178.

[5] Zhao, C.; Xu, G. L.; Yu, Z.; Zhang, L. C.; Hwang, I.; Mo, Y. X.; Ren, Y. X.; Cheng, L.; Sun, C. J.; Ren, Y. et al. A high-energy and long-cycling lithium-sulfur pouch cell via a macroporous catalytic cathode with double-end binding sites. *Nat. Nanotechnol.* **2021**, *16*, 166–173.

[6] Ye, Z. Q.; Jiang, Y.; Li, L.; Wu, F.; Chen, R. J. Self-assembly of 0D-2D heterostructure electrocatalyst from MOF and MXene for boosted lithium polysulfide conversion reaction. *Adv. Mater.* **2021**, *33*, 2101204.

[7] Shaibani, M.; Mirshekarloo, M. S.; Singh, R.; Easton, C. D.; Cooray, M. C. D.; Eshraghi, N.; Abendroth, T.; Dörfler, S.; Althues, H.; Kaskel, S. et al. Expansion-tolerant architectures for stable cycling of ultrahigh-loading sulfur cathodes in lithium-sulfur batteries. *Sci. Adv.* **2020**, *6*, eaay2757.

[8] Li, S. L.; Zhang, W. F.; Zheng, J. F.; Lv, M. Y.; Song, H. Y.; Du, L. Inhibition of polysulfide shuttles in Li-S batteries: Modified separators and solid-state electrolytes. *Adv. Energy Mater.* **2021**, *11*, 2000779.

[9] Manthiram, A.; Fu, Y. Z.; Chung, S. H.; Zu, C. X.; Su, Y. S. Rechargeable lithium-sulfur batteries. *Chem. Rev.* **2014**, *114*, 11751–11787.

[10] Peng, L. L.; Wei, Z. Y.; Wan, C. Z.; Li, J.; Chen, Z.; Zhu, D.; Baumann, D.; Liu, H. T.; Allen, C. S.; Xu, X. et al. A fundamental look at electrocatalytic sulfur reduction reaction. *Nat. Catal.* **2020**, *3*, 762–770.

[11] Qian, J.; Xing, Y.; Yang, Y.; Li, Y.; Yu, K. X.; Li, W. L.; Zhao, T.; Ye, Y. S.; Li, L.; Wu, F. et al. Enhanced electrochemical kinetics with highly dispersed conductive and electrocatalytic mediators for lithium-sulfur batteries. *Adv. Mater.* **2021**, *33*, 2100810.

[12] Sun, Z. H.; Zhang, J. Q.; Yin, L. C.; Hu, G. J.; Fang, R. P.; Cheng, H. M.; Li, F. Conductive porous vanadium nitride/graphene composite as chemical anchor of polysulfides for lithium-sulfur batteries. *Nat. Commun.* **2017**, *8*, 14627.

[13] He, J. R.; Chen, Y. F.; Manthiram, A. Vertical Co_9S_8 hollow nanowall arrays grown on a Celgard separator as a multifunctional polysulfide barrier for high-performance Li-S batteries. *Energy Environ. Sci.* **2018**, *11*, 2560–2568.

[14] Huang, X. Z.; He, R.; Li, M.; Chee, M. O. L.; Dong, P.; Lu, J. Functionalized separator for next-generation batteries. *Mater. Today* **2020**, *41*, 143–155.

[15] Zhou, C.; Li, Z. H.; Xu, X.; Mai, L. Q. Metal-organic frameworks enable broad strategies for lithium-sulfur batteries. *Natl. Sci. Rev.* **2021**, *8*, nwab055.

[16] Knebel, A.; Bavykina, A.; Datta, S. J.; Sundermann, L.; Garzon-Tovar, L.; Lebedev, Y.; Durini, S.; Ahmad, R.; Kozlov, S. M.; Shterk, G. et al. Solution processable metal–organic frameworks for mixed matrix membranes using porous liquids. *Nat. Mater.* **2020**, *19*, 1346–1353.

[17] Li, C. E.; Liu, J. H.; Zhang, K. X.; Zhang, S. W.; Lee, Y.; Li, T. Coating the right polymer: Achieving ideal metal–organic framework particle dispersibility in polymer matrixes using a coordinative crosslinking surface modification method. *Angew. Chem., Int. Ed.* **2021**, *60*, 14138–14145.

[18] Liang, Z. B.; Qu, C.; Guo, W. H.; Zou, R. Q.; Xu, Q. Pristine metal–organic frameworks and their composites for energy storage and conversion. *Adv. Mater.* **2018**, *30*, 1702891.

[19] Wang, Z. S.; Shen, J. D.; Liu, J.; Xu, X. J.; Liu, Z. B.; Hu, R. Z.; Yang, L. C.; Feng, Y. Z.; Liu, J.; Shi, Z. C. et al. Self-supported and flexible sulfur cathode enabled via synergistic confinement for high-energy-density lithium-sulfur batteries. *Adv. Mater.* **2019**, *31*, 1902228.

[20] Ye, Z. Q.; Jiang, Y.; Qian, J.; Li, W. L.; Feng, T.; Li, L.; Wu, F.; Chen, R. J. Exceptional adsorption and catalysis effects of hollow polyhedra/carbon nanotube confined CoP nanoparticles superstructures for enhanced lithium-sulfur batteries. *Nano Energy* **2019**, *64*, 103965.

[21] Yang, D. W.; Liang, Z. F.; Tang, P. Y.; Zhang, C. Q.; Tang, M. X.; Li, Q. Z.; Biendicho, J. J.; Li, J. S.; Heggen, M.; Dunin-Borkowski, R. E. et al. A high conductivity 1D π–d conjugated metal–organic framework with efficient polysulfide trapping-diffusion-catalysis in lithium-sulfur batteries. *Adv. Mater.* **2022**, *34*, 2108835.

[22] Wu, F.; Zhao, S. Y.; Chen, L.; Lu, Y.; Su, Y. F.; Jia, Y. N.; Bao, L. Y.; Wang, J.; Chen, S.; Chen, R. J. Metal–organic frameworks composites threaded on the CNT knitted separator for suppressing the shuttle effect of lithium sulfur batteries. *Energy Storage Mater.* **2018**, *14*, 383–391.

[23] Chen, K.; Sun, Z. H.; Fang, R. P.; Shi, Y.; Cheng, H. M.; Li, F. Metal–organic frameworks (MOFs)-derived nitrogen-doped porous carbon anchored on graphene with multifunctional effects for lithium-sulfur batteries. *Adv. Funct. Mater.* **2018**, *28*, 1707592.

[24] Li, W. T.; Guo, X. T.; Geng, P. B.; Du, M.; Jing, Q. L.; Chen, X. D.; Zhang, G. X.; Li, H. P.; Xu, Q.; Braunstein, P. et al. Rational design and general synthesis of multimetallic metal–organic framework nano-octahedra for enhanced Li-S battery. *Adv. Mater.* **2021**, *33*, 2105163.

[25] Liu, B. R.; Taheri, M.; Torres, J. F.; Fusco, Z.; Lu, T.; Liu, Y.; Tsuzuki, T.; Yu, G. H.; Tricoli, A. Janus conductive/insulating microporous ion-sieving membranes for stable Li-S batteries. *ACS Nano* **2020**, *14*, 13852–13864.

[26] Gu, S. H.; Jiang, H. L.; Li, X. C.; Dai, Y.; Zheng, W. J.; Jiang, X. B.; He, G. H. Dispersing single-layered $Ti_3C_2T_x$ nanosheets in hierarchically-porous membrane for high-efficiency Li^+ transporting and polysulfide anchoring in Li-S batteries. *Energy Storage Mater.* **2022**, *53*, 32–41.

[27] Huang, X.; Tang, J. Y.; Luo, B.; Knibbe, R.; Lin, T.; Hu, H.; Rana, M.; Hu, Y. X.; Zhu, X. B.; Gu, Q. F. et al. Sandwich-like ultrathin TiS_2 nanosheets confined within N, S codoped porous carbon as an effective polysulfide promoter in lithium-sulfur batteries. *Adv. Energy Mater.* **2019**, *9*, 1901872.

[28] Wei, C. L.; Wang, Y. S.; Zhang, Y. C.; Tan, L. W.; Qian, Y.; Tao, Y.; Xiong, S. L.; Feng, J. K. Flexible and stable 3D lithium metal anodes based on self-standing MXene/COF frameworks for high-performance lithium-sulfur batteries. *Nano Res.* **2021**, *14*, 3576–3584.

[29] Xiong, D. B.; Shi, Y. M.; Yang, H. Y. Rational design of MXene-based films for energy storage: Progress, prospects. *Mater. Today* **2021**, *46*, 183–211.

[30] Zhao, M. Q.; Sedran, M.; Ling, Z.; Lukatskaya, M. R.; Mashtalir, O.;

Ghidiu, M.; Dyatkin, B.; Tallman, D. J.; Djenizian, T.; Barsoum, M. W. et al. Synthesis of carbon/sulfur nanolaminates by electrochemical extraction of titanium from Ti$_2$SC. *Angew. Chem., Int. Ed.* **2015**, *54*, 4810–4814.

[31] Zhou, C.; Li, M.; Hu, N. T.; Yang, J. H.; Li, H.; Yan, J. W.; Lei, P. Y.; Zhuang, Y. P.; Guo, S. W. Single-atom-regulated heterostructure of binary nanosheets to enable dendrite-free and kinetics-enhanced Li-S batteries. *Adv. Funct. Mater.* **2022**, *32*, 2204635.

[32] Zhuang, Z. C.; Xia, L. X.; Huang, J. Z.; Zhu, P.; Li, Y.; Ye, C. L.; Xia, M. G.; Yu, R. H.; Lang, Z. Q.; Zhu, J. X. et al. Continuous modulation of electrocatalytic oxygen reduction activities of single-atom catalysts through p-n junction rectification. *Angew. Chem., Int. Ed.* **2023**, *62*, e202212335.

[33] Liu, Z. H.; Du, Y.; Yu, R. H.; Zheng, M. B.; Hu, R.; Wu, J. S.; Xia, Y. Y.; Zhuang, Z. C.; Wang, D. S. Tuning mass transport in electrocatalysis down to sub-5 nm through nanoscale grade separation. *Angew. Chem.* **2023**, *62*, e202212653.

[34] Zhang, E. H.; Hu, X.; Meng, L. Z.; Qiu, M.; Chen, J. X.; Liu, Y. J.; Liu, G. Y.; Zhuang, Z. C.; Zheng, X. B.; Zheng, L. R. et al. Single-atom yttrium engineering Janus electrode for rechargeable Na-S batteries. *J. Am. Chem. Soc.* **2022**, *144*, 18995–19007.

[35] Jiang, J. Z.; Bai, S. S.; Zou, J.; Liu, S.; Hsu, J. P.; Li, N.; Zhu, G. Y.; Zhuang, Z. C.; Kang, Q.; Zhang, Y. Z. Improving stability of MXenes. *Nano Res.* **2022**, *15*, 6551–6567.

[36] Liu, Z. H.; Du, Y.; Zhang, P. F.; Zhuang, Z. C.; Wang, D. S. Bringing catalytic order out of chaos with nitrogen-doped ordered mesoporous carbon. *Matter* **2021**, *4*, 3161–3194.

[37] Jiao, L.; Zhang, C.; Geng, C. N.; Wu, S. C.; Li, H.; Lv, W.; Tao, Y.; Chen, Z. J.; Zhou, G. M.; Li, J. et al. Capture and catalytic conversion of polysulfides by *in situ* built TiO$_2$-MXene heterostructures for lithium-sulfur batteries. *Adv. Energy Mater.* **2019**, *9*, 1900219.

[38] Zhang, S. Z.; Zhong, N.; Zhou, X.; Zhang, M. J.; Huang, X. P.; Yang, X. L.; Meng, R. J.; Liang, X. Comprehensive design of the high-sulfur-loading Li-S battery based on MXene nanosheets. *Nano-Micro Lett.* **2020**, *12*, 112.

[39] Malik, R. Maxing out water desalination with MXenes. *Joule* **2018**, *2*, 591–593.

[40] Qian, X. J.; Fan, X. Q.; Peng, Y. L.; Xue, P.; Sun, C.; Shi, X. L.; Lai, C.; Liang, J. J. Polysiloxane cross-linked mechanically stable MXene-based lithium host for ultrastable lithium metal anodes with ultrahigh current densities and capacities. *Adv. Funct. Mater.* **2021**, *31*, 2008044.

[41] Shin, H.; Eom, W.; Lee, K. H.; Jeong, W.; Kang, D. J.; Han, T. H. Highly electroconductive and mechanically strong Ti$_3$C$_2$T$_x$ MXene fibers using a deformable mxene gel. *ACS Nano* **2021**, *15*, 3320–3329.

[42] Wu, Y. C.; Wei, W.; Yu, R. H.; Xia, L. X.; Hong, X. F.; Zhu, J. X.; Li, J. T.; Lv, L.; Chen, W.; Zhao, Y. et al. Anchoring sub-nanometer Pt clusters on crumpled paper-like MXene enables high hydrogen evolution mass activity. *Adv. Funct. Mater.* **2022**, *32*, 2110910.

[43] Rodenas, T.; Luz, I.; Prieto, G.; Seoane, B.; Miro, H.; Corma, A.; Kapteijn, F.; Llabrés I Xamena, F. X.; Gascon, J. Metal–organic framework nanosheets in polymer composite materials for gas separation. *Nat. Mater* **2015**, *14*, 48–55.

[44] Naguib, M.; Kurtoglu, M.; Presser, V.; Lu, J.; Niu, J. J.; Heon, M.; Hultman, L.; Gogotsi, Y.; Barsoum, M. W. Two-dimensional nanocrystals produced by exfoliation of Ti$_3$AlC$_2$. *Adv. Mater.* **2011**, *23*, 4248–4253.

[45] Zhao, L.; Dong, B. L.; Li, S. Z.; Zhou, L. J.; Lai, L. F.; Wang, Z. W.; Zhao, S. L.; Han, M.; Gao, K.; Lu, M. et al. Interdiffusion reaction-assisted hybridization of two-dimensional metal–organic frameworks and Ti$_3$C$_2$T$_x$ nanosheets for electrocatalytic oxygen evolution. *ACS Nano* **2017**, *11*, 5800–5807.

[46] Shi, M. J.; Liu, Z.; Zhang, S.; Liang, S. C.; Jiang, Y. T.; Bai, H.; Jiang, Z. M.; Chang, J.; Feng, J.; Chen, W. S. et al. A Mott–Schottky heterogeneous layer for Li-S batteries: Enabling both high stability and commercial-sulfur utilization. *Adv. Energy Mater.* **2022**, *12*, 2103657.

[47] Sun, R.; Bai, Y.; Bai, Z.; Peng, L.; Luo, M.; Qu, M. X.; Gao, Y. C.; Wang, Z. H.; Sun, W.; Sun, K. N. Phosphorus vacancies as effective polysulfide promoter for high-energy-density lithium-sulfur batteries. *Adv. Energy Mater.* **2022**, *12*, 2102739.

[48] Ren, Y. L.; Zhai, Q. X.; Wang, B.; Hu, L. B.; Ma, Y. J.; Dai, Y. M.; Tang, S. C.; Meng, X. K. Synergistic adsorption-electrocatalysis of 2D/2D heterostructure toward high performance Li-S batteries. *Chem. Eng. J.* **2022**, *439*, 135535.

[49] Ma, F.; Srinivas, K.; Zhang, X.; Zhang, Z.; Wu, Y.; Liu, D.; Zhang, W.; Wu, Q.; Chen, Y. Mo$_2$N quantum dots decorated N-doped graphene nanosheets as dual-functional interlayer for dendrite-free and shuttle-free lithium-sulfur batteries. *Adv. Funct. Mater.* **2022**, *32*, 2206113.

[50] Yao, W. Q.; Tian, C. X.; Yang, C.; Xu, J.; Meng, Y. F.; Manke, I.; Chen, N.; Wu, Z. L.; Zhan, L.; Wang, Y. L. et al. P-doped NiTe$_2$ with Te-vacancies in lithium-sulfur batteries prevents shuttling and promotes polysulfide conversion. *Adv. Mater.* **2022**, *34*, 2106370.

[51] Yao, W. Q.; Xu, J.; Cao, Y. J.; Meng, Y. F.; Wu, Z. L.; Zhan, L.; Wang, Y. L.; Zhang, Y. L.; Manke, I.; Chen, N. et al. Dynamic intercalation-conversion site supported ultrathin 2D mesoporous SnO$_2$/SnSe$_2$ hybrid as bifunctional polysulfide immobilizer and lithium regulator for lithium-sulfur chemistry. *ACS Nano* **2022**, *16*, 10783–10797.